

# Explicit symplectic integrators with adaptive time steps in curved spacetimes

Xin Wu<sup>1,\*</sup>, Ying Wang<sup>1</sup>, Wei Sun<sup>1</sup>, Fuyao Liu<sup>1</sup>, Dazhu Ma<sup>2</sup>

1. Center of Application and Research of Computational Physics & School of Mathematics, Physics and Statistics, Shanghai University of Engineering Science, Shanghai 201620, China

2. College of Intelligent Systems Science and Engineering, Hubei Minzu University, Enshi 445000, China

Emails: \*wuxin\_1134@sina.com (X. W.)

## ABSTRACT

Recently, our group developed explicit symplectic methods for curved spacetimes that are not split into several explicitly integrable parts, but are via appropriate time transformations. Such time-transformed explicit symplectic integrators should have employed adaptive time steps in principle, but they are often difficult in practical implementations. In fact, they work well if time transformation functions cause the time-transformed Hamiltonians to have the desired splits and approach 1 or constants for sufficiently large distances. However, they do not satisfy the requirement of step-size selections in this case. Based on the step-size control technique proposed by Preto & Saha, the nonadaptive time step time-transformed explicit symplectic methods are slightly adjusted as adaptive ones. The adaptive methods have only two additional steps and a negligible increase in computational cost as compared with the nonadaptive ones. Their implementation is simple. Several dynamical simulations of particles and photons near black holes have demonstrated that the adaptive methods typically improve the efficiency of the nonadaptive methods. Because of the desirable property, the new adaptive methods are applied to investigate the chaotic dynamics of particles and photons outside the horizon in a Schwarzschild-Melvin spacetime. The new methods are widely applicable to all curved spacetimes corresponding to Hamiltonians or time-transformed Hamiltonians with the expected splits. Also application to the backwards ray-tracing method for studying the motion of photons and shadows of black holes is possible.

*Unified Astronomy Thesaurus concepts:* Black hole physics (159); Computational methods (1965); Computational astronomy (293); Celestial mechanics (211)

## 1. Introduction

In recent several years, the shadow image of the supermassive black hole in the core of the elliptical galaxy M87\* has been detected by the Event Horizon Telescope (EHT Collaboration et al. 2019). The result is extremely consistent with that predicted by Einstein's Theory of General Relativity. The black hole image is formed due to the significant gravitational lensing effect of nearby radiation under the extremely strong gravity interaction of the black hole. It is the lensed image at infinity of the photon sphere, which corresponds to the boundary between photon orbits escaping to infinity and photon orbits falling into the black hole (Virbhadrha 2024).

In fact, the black hole shadows are located at the

region in the observer sky corresponding to photon orbits that spiral toward into the black hole. In this sense, computations of black hole shadows are attributed to studying the motion of photons outside the horizons of black holes and finding the correspondence between the falling light rays and the points in the sky. For integrable spacetimes (e.g. the Kerr metric), analytical methods can accurately provide the shadow edges like the photon sphere (Bardeen & Cunningham 1973). However, no analytical methods but numerical ones can carry out this task in the general cases (in particular for nonintegrable spacetimes). Through numerically backward integrations of the geodesic equations of the light rays from the observer, one traces the evolution of the light rays and identifies which of the light rays from the observer fall into the center. This is a backward ray-tracing method (Johannsen 2013). Because the final evolutions of numerous points corresponding to photon orbits in the sky are numerically traced, the computations are hopelessly expensive. To save la-

bor and to possess high accuracy, an explicit integrator is necessary to employ large time steps when an orbit runs far away from the black hole, but small ones when the orbit is close to the horizon of the black hole. That is, adaptive time steps with the desired stretching and shrinking are needed in the numerical integration scheme. Due to this advantage, adaptive time steps were added to fifth-order Runge-Kutta schemes (Pu et al. 2016; White 2022), Adams-Moulton method (Pelle et al. 2022), eight-order embedded Runge-Kutta method (Kawashima et al. 2023) and fourth-order Runge-Kutta-Fehlberg algorithm (Younsi et al. 2023) in these ray-tracing codes.

The integration schemes adopted in the existing ray-tracing methods as traditional solvers should have no problems in the description of photon motions and black hole shadows when the integration times are short. However, they would provide unreliable results for long-term simulations because they lack the constancy of the integrals of motion and the preservation of symplectic structure which conservative Hamiltonian systems possess. It is possible for a photon to slowly fall into a black hole or to slowly scatter to infinity in some cases, e.g. the presence of weak chaotic behavior in a nonintegrable spacetime. Thus, long-term integration of the photon orbit is required for the identification of the final state of the photon orbit. In fact, many curved spacetimes can become Hamiltonian problems. The most appropriate solvers for Hamiltonian systems are symplectic methods which respect the inherent canonical nature of the original Hamiltonian dynamics (Wisdom 1982; Ruth 1983; Feng 1986). They show no secular errors in the integrals of motion such as the conserved energy. They make the energy oscillatory but not be exact conservation. An integrator with both symplecticity and exact energy conservation is rare. Although an exactly energy-conserving implicit integration scheme with the preservation of the underlying Hamiltonian was given by Bacchini et al. (2019a, b), it is not symplectic.

The Hamiltonian systems for curved spacetimes are not separable to the variables and cannot be split into two terms that are explicitly solvable. In this case, explicit symplectic integrators seem to become useless. Instead, implicit symplectic integrators can be applied for curved spacetimes (Brown 2006; Kopáček et al. 2010; Seyrich & Lukes-Gerakopoulos 2012; Tsang et al. 2015). Semiexplicit symplectic methods for inseparable Hamiltonian systems (Jayawardana & Oh-

sawa 2023; Ohsawa 2023) can also be. They were developed along the extended phase space method of Pihajoki (2015), and are symplectic not only in the extended phase space but also in the original phase space. The explicit methods are less computationally demanding than the implicit ones. Recently, our group showed that the Hamiltonian systems of some curved spacetimes such as the Schwarzschild metric can be separated into three or more explicitly solvable parts (Wang et al. 2021a, b, c; Zhou et al. 2022, 2023). In this way, explicit symplectic methods are easily implemented. However, some other curved spacetimes like the Kerr metric have no such desirable splits. Wu et al. (2021, 2022) found that the construction of explicit symplectic methods for these curved spacetimes is still possible according to the idea of time transformation considered by Mikkola (1997). Such time-transformed explicit symplectic integrators were applied to study the chaotic dynamics of particles near a magnetic deformed Schwarzschild black hole (Huang et al. 2022). Constant step sizes are adopted for the newly transformed time in the methods, and do not break the symplectic property. Although the established time-transformed explicit symplectic integrators allow for the application of adaptive time steps to the original time, they have some difficulty in the implementation due to a great deal of computational cost. The time transformation functions for constructing efficient explicit symplectic algorithms are close to 1 or constants in general when the distances are large enough. This means that the original time and the new time are almost the same, and the original time steps remain approximately constant.

Of course, the time-transformed explicit symplectic integrators allow for the use of adaptive time steps in the work of Mikkola (1997). Such time transformation method is applied to improve the efficiency of the symplectic leapfrog algorithm of Wisdom & Holman (1991) for highly eccentric orbits and close encounters between objects in various few-body problems in the Solar System. The logarithmic-Hamiltonian leapfrog algorithm is also an efficient adaptive time step symplectic method for  $N$ -body problems (Mikkola & Tanikawa 1999, 2013). A class of adaptive time step, reversible, explicit symplectic integration algorithms were formulated for the long-term integration of nearly Keplerian orbits in separable Hamiltonian systems (Preto & Tremaine 1999). Emel'yanenko (2007) developed an explicit symplectic method that allows individual adaptive time-steps in long-term in-

tegrations of the planetary N-body problem. Following the derivation of Emel'yanenko (2007), Preto & Saha (2009) provided a symplectic scheme with adaptive time steps for a post-Newtonian Hamiltonian from the Kerr metric. This method is an explicitly and implicitly combined algorithm. In the method, a auxiliary variable  $\Phi$  is used as a conjugate momentum with respect to the original time being an additional coordinate.  $\Phi$  is kept constant during the calculation of the other coordinates and momenta in every integration step, whereas it is advanced after the step integration ends. In fact,  $\Phi$  acts as a rescaled factor for adjusting the time variables.

Combining the expected time transformation functions suggested by Wu et al. (2021, 2022) and the auxiliary variable  $\Phi$  introduced by Preto & Saha (2009), we design an adaptive time step explicit symplectic integrator for curved spacetimes. This is the main attempt of the present paper. For the sake of this aim, we describe the new adaptive time step explicit symplectic integrator in Section 2. Then, the motions of particles and photons around several black holes are used to show efficient implementation of the new algorithm and to test the performance of the new algorithm in Section 3. The applicability of the new method to the chaotic dynamics of particles and photons near a Schwarzschild-Melvin black hole (Ernst 1976) is also considered. Finally, the main results are concluded in Section 4. Possible choices of time transformation functions for several curved spacetimes are given in Appendix A.

## 2. Adaptive time step explicit symplectic integrators in curved spacetimes

Consider that an axial-symmetric rotating black hole geometry in the Boyer-Lindquist coordinates  $(t, r, \theta, \phi)$  corresponds to the covariant metric

$$\begin{aligned} dS^2 &= g_{\alpha\beta} dx^\alpha dx^\beta \\ &= g_{tt} dt^2 + 2g_{t\phi} dt d\phi + g_{rr} dr^2 \\ &\quad + g_{\theta\theta} d\theta^2 + g_{\phi\phi} d\phi^2. \end{aligned} \quad (1)$$

The metric components  $g_{tt}, \dots, g_{\phi\phi}$  are functions of the two variables  $r$  and  $\theta$ . This metric has contravariant nonzero components

$$\begin{aligned} g^{tt} &= \frac{g_{\phi\phi}}{g_{tt}g_{\phi\phi} - g_{t\phi}^2}, & g^{t\phi} &= \frac{g_{t\phi}}{g_{t\phi}^2 - g_{tt}g_{\phi\phi}}, \\ g^{\phi\phi} &= \frac{g_{tt}}{g_{tt}g_{\phi\phi} - g_{t\phi}^2}, & g^{rr} &= \frac{1}{g_{rr}}, & g^{\theta\theta} &= \frac{1}{g_{\theta\theta}}. \end{aligned}$$

The geodesic motion of a massive test particle or massless photon in this spacetime is described by a Hamiltonian system with two degrees of freedom

$$H = \frac{1}{2} g^{\alpha\beta} p_\alpha p_\beta = f(r, \theta) + \frac{1}{2} g^{rr} p_r^2 + \frac{1}{2} g^{\theta\theta} p_\theta^2, \quad (2)$$

where  $f(r, \theta)$  is a function of  $r$  and  $\theta$  in the form

$$f(r, \theta) = \frac{1}{2} (g^{tt} E^2 + g^{\phi\phi} L^2) - g^{t\phi} EL. \quad (3)$$

$p_r$  and  $p_\theta$  are the covariant momenta with respect to  $r$  and  $\theta$ . The metric components do not explicitly depend on  $t$  and  $\phi$ , therefore, the specific energy  $E$  and angular momentum  $L$  of the particle or photon are two constants of motion, which correspond to the covariant momenta  $p_t = -E$  and  $p_\phi = L$ . Due to the particle's or photon's rest mass, the Hamiltonian is also a constant of motion:

$$H = -p_0, \quad (4)$$

where  $p_0 = 1/2$  for the time-like geodesics but  $p_0 = 0$  for the null geodesics. Here, the speed of light  $c$  and the gravitational constant  $G$  are taken as geometrized units,  $c = G = 1$ .

### 2.1. Comments on the existing time-transformed explicit symplectic integrators without adaptive time steps

Unlike the Hamiltonian systems of nonrotating black holes such as the Schwarzschild black hole (Wang et al. 2021a), the Hamiltonian system (2) for the rotating black holes like the Kerr black hole is not directly split into several explicit integrable pieces in general. This seems to show that explicit symplectic methods become useless in the system (2). However, this problem may be solved with the aid of the idea of time transformations for constructing efficient symplectic algorithms proposed by Mikkola (1997). Wu et al. (2021) found an appropriate time transformation function to the Hamiltonian of Kerr geometry so that the obtained time-transformed Hamiltonian has three or more splitting parts which are explicitly solvable. Through such time transformations and symplectic splitting methods, symmetric compositions can yield explicit symplectic integrators. A possible path on the construction of time-transformed explicit symplectic schemes for the Hamiltonian (2) is introduced simply as follows.

Set  $\tau$  as a physical time variable. It denotes the proper time for the time-like geodesic motion, and is

an affine time parameter for the null geodesic motion. Suppose that  $w$  is a new time variable different from the coordinate time  $t$ . The old time  $\tau$  and the new time  $w$  satisfy the relation

$$d\tau = g(r, \theta)dw, \quad (5)$$

where  $g(r, \theta)$  is a time transformation function depending on  $r$  and  $\theta$ . This function should be chosen appropriately so that the time-transformed Hamiltonian

$$\begin{aligned} K &= g(r, \theta)(H + p_0) \\ &= g(r, \theta)(f(r, \theta) + p_0) + \frac{1}{2}g(r, \theta)g^{rr}p_r^2 \\ &\quad + \frac{1}{2}g(r, \theta)g^{\theta\theta}p_\theta^2 \end{aligned} \quad (6)$$

consists of several terms having analytical solutions as explicit functions of the new time  $w$ . In fact, the second, third terms of Equation (6) should be required to have the explicitly integrable splits.  $p_0$  in Equation (6) is the same as that in Equation (4) and represents a momentum corresponding to a coordinate  $q_0 = \tau$ .<sup>1</sup> The Hamiltonian  $H + p_0$  is based on the use of the extended phase space. Because  $H + p_0 = 0$ ,  $K$  is always identical to zero for any new time  $w$ , i.e.  $K = 0$ . Via these operations, the time-transformed Hamiltonian (6) has the splitting expression

$$K = \sum_{i=1}^l K_i. \quad (7)$$

Now, let symplectic operators  $\psi_i$  be analytical solvers of the sub-Hamiltonians  $K_i$ . Composing these symplectic operators results in a first-order approximation to the exact solution of the Hamiltonian (6):

$$\chi(h) = \psi_l^h \times \cdots \times \psi_1^h, \quad (8)$$

where  $h$  is a time step of the new time  $w$ . The operator  $\chi$  corresponds to its adjoint

$$\chi^*(h) = \psi_1^h \times \cdots \times \psi_l^h. \quad (9)$$

In terms of the two operators, a second-order explicit symplectic method

$$S_2(h) = \chi\left(\frac{h}{2}\right) \times \chi^*\left(\frac{h}{2}\right) \quad (10)$$

is symmetrically designed for the Hamiltonian (6) or (7). The second-order method can easily compose higher-order explicit symplectic integration algorithms (Yoshida 1990; Blanes & Moan 2002; Blanes et al. 2008, 2010; Blanes et al. 2024). These algorithms use fixed time steps in the new time, but may adopt variable ones in the old time. This treatment is helpful to preserve the symplectic structure of the Hamiltonian (6) in the new time.

Clearly, how to find a suitable time transformation function and how to split the time-transformed Hamiltonian are two keys for the application of explicit symplectic integrators to the Hamiltonian (2). In particular, the time transformation function is useful to eliminate some factors in the second, third terms of the inseparable Hamiltonian (2) so that the left second, third terms satisfy the desired splitting needs. Some examples are listed here. For the Kerr black hole with the spin angular momentum  $a$ , Wu et al. (2021) gave the time transformation function by

$$g(r, \theta) = \frac{\Sigma}{r^2} = \frac{1}{r^2}(r^2 + a^2 \cos^2 \theta), \quad (11)$$

and split the time-transformed Hamiltonian into five explicitly integrable pieces. For other curved spacetimes such as the rotating black ring, regular black holes, Gauss-Bonnet black hole, majumdar-Papapetrou dihole black holes, relativistic core-shell models and Kerr-Newman solution with disformal parameter, the time transformation functions and splitting Hamiltonian methods were also given by Wu et al. (2022). A notable point is that all the time transformation functions chosen in the two works of Wu et al. (2021, 2022) are nearly equal to 1 for sufficiently large radial distances  $r$ , i.e.  $g(r, \theta) \rightarrow 1$  as  $r \rightarrow \infty$ . In other words, the old time step  $\Delta\tau$  is almost consistent with the new time step  $\Delta w = h$ . As a result, both the old time  $\tau$  and the new time  $w$  have no typical differences. No adaptive time steps are employed for the old time when a fixed time step is used for the new time. This result was shown numerically in Figure 5b of Wu et al. (2021).

In principle, it should be admissible to replace the time transformation function (11) with other functions, as was claimed by Wu et al. (2021). For instance, the time transformation function is taken as

$$g_1 = rg(r, \theta) = r + \frac{a^2}{r} \cos^2 \theta, \quad (12)$$

or

$$g_2 = r^2 g(r, \theta) = r^2 + a^2 \cos^2 \theta. \quad (13)$$

<sup>1</sup>This means the old time  $\tau$  treated as an additional coordinate.

Seen from a theoretical point of view, the choice of the time transformation function  $g_1$  or  $g_2$  can allow for the application of explicit symplectic integrators in the Kerr spacetime without doubt. In this case, the established explicit symplectic methods like  $S_2$  use adaptive time steps for the old time. This point is illustrated here. When the separation  $r$  is large enough,  $g_1 \sim r$  and  $g_2 \sim r^2$ ; namely,  $d\tau \approx rdw$  for the use of  $g_1$  and  $d\tau \approx r^2dw$  for the use of  $g_2$ . Thus, the original time-step selection is mainly controlled by the radial distance  $r$ . For the use of constant new time step  $h$ , the old time step  $\Delta\tau$  is typically variable because it decreases as a particle goes towards the black hole, whereas increases when the particle runs away from the black hole. For a small radial separation  $r$ , shortening of step sizes is useful to improve the treatment of highly eccentric orbits or close encounters. For a large radial separation  $r$ , enlarging of step sizes is good to save computational cost. That is to say, the old time steps  $\Delta\tau$  have the desired stretching and shrinking. Nevertheless, this does not lead to breaking the symplectic property of the Hamiltonian (6) because the new time step  $h$  remains fixed. In a word, improving accuracy and saving labors are the benefits of adaptive time-step controls. Unfortunately, the implementation of such adaptive time step explicit symplectic integrators for the choice of  $g_1$  or  $g_2$  is rather cumbersome from practical computations because the smaller original time-step selection requires choosing a much shorter new time step  $h$ , and would lead to a great deal of computational cost as well as numerous round-off errors.

Perhaps someone wants to know whether the performance of  $S_2$  becomes better when the time transformation function  $g_1$  gives place to another form

$$g^* = \frac{r}{j}g, \quad (14)$$

where  $j$  is a free parameter and  $j \geq r_{max}^2$  is possibly admitted. Although an appropriately large new time step  $h$  (e.g.  $h = 1$ ) can make the old time step  $\Delta\tau$  be extremely small in this case, the computations are still more expensive and fail to yield putouts. A possible reason for the algorithm  $S_2$  not retaining the great speed advantage of conventional symplectic integrators is that the factor  $r/j$  in Equation (14) is not only a rescaled time variable but also affects the differential equations for the motion. If the role of  $r/j$  is only a rescaled time factor for adjusting the time-

<sup>2</sup> $r_{max}$  is the maximum value of  $r$  in a bounded orbit.

step in integrations and does not change the Hamiltonian canonical equations of motion, then the adaptive time step explicit symplectic integrator  $S_2$  for the use of  $g^*$  would work well. In what follows, we discuss the possibility of the function  $r/j$  that is only viewed as a rescaled time factor.

## 2.2. Efficient implementation of new adaptive time step explicit symplectic integrator

As is mentioned above, the implementation of the highly efficient explicit symplectic integrators such as  $S_2$  requires that the time transformation function  $g$  of Equation (5) should satisfy two points. One point is that the time transformation function can successfully eliminate some factors impeding the second, third terms of the Hamiltonian (2) so that the Hamiltonian (6) is split into several explicitly integrable parts. The other point is that  $g \approx 1$  as the radial separation  $r$  is sufficiently large. On the other hand, Emel'yanenko (2007) derived an elegant Hamiltonian of adaptive stepsize. Following the Hamiltonian derivation, Preto & Saha (2009) developed a symplectic integrator with adaptive time steps for fast and accurate numerical calculation of a post-Newtonian Hamiltonian describing the motion of a test particle in a Kerr metric. In the algorithmic construction, they introduced a conjugate momentum  $\Phi$  with respect to the additional coordinate  $\tau$  as a rescaled time variable adjusting the time steps in integrations.<sup>3</sup> In addition, the Keplerian part as the main part of the Hamiltonian is solved analytically using the algorithmic regularization scheme of Preto & Tremaine (1999), and the perturbation part consisting of post-Newtonian and external potential terms is calculated by the implicit midpoint method (i.e. a second order symplectic integrator) of Feng (1986). Composing the explicitly analytical solution and the implicitly numerical solution produces a generalized leapfrog. This is the idea of Preto & Saha (2009) about the construction of adaptive time step symplectic integrator. Now, combining the expected time transformation function  $g$  and the rescaled time variable  $\Phi$ , we design an adaptive time step explicit symplectic integrator for the Hamiltonian (2).

Transforming from the old time  $\tau$  to a new independent time variable  $s$ , i.e.  $\tau \rightarrow s$  (the relation between the two times is subsequently derived), we use  $g$  and

<sup>3</sup>The conjugate momentum of the coordinate  $\tau$  is  $p_0$  in Equation (6). However, it is here that the conjugate momentum is  $\Phi$  and  $p_0$  is only the constant 1/2 or 0 in Equation (4).

$\Phi$  to readjust the Hamiltonian (2) or to slightly modify the Hamiltonian (6) as

$$\begin{aligned} F &= \frac{K}{\Phi} + g \ln \left( \frac{\Phi}{\varphi(\tau)} \right) \\ &= \frac{g}{\Phi} (H + p_0) + g \ln \left( \frac{\Phi}{\varphi(\tau)} \right) \\ &= \frac{1}{\Phi} \sum_{i=1}^l K_i + g \ln \left( \frac{\Phi}{\varphi(\tau)} \right), \end{aligned} \quad (15)$$

where  $\varphi(\tau) = \varphi(r(\tau), \theta(\tau))$  is a given function of the original time  $\tau$ .<sup>4</sup> If  $g = 1$ , line 2 of Equation (15) is Equation (21) of Preto & Saha (2009).

When a set of solutions  $r$ ,  $\theta$ ,  $p_r$  and  $p_\theta$  are obtained from the first term<sup>5</sup> of line 3 in Equation (15),  $\Phi$  remains constant. In this case, they are still given by the algorithm  $S_2(h)$  in Equation (10), but  $h$  should be adjusted as  $h/\Phi$ . Namely,  $S_2(h/\Phi)$  provides the solutions  $r$ ,  $\theta$ ,  $p_r$  and  $p_\theta$  at some time  $s$ . Note that  $\Phi$  is viewed as a constant only in computing the solutions  $r$ ,  $\theta$ ,  $p_r$  and  $p_\theta$ , but varies with time  $s$  after one step integration according to one of Hamilton's equations for  $F$ :

$$\frac{d\Phi}{ds} = -\frac{\partial F}{\partial \tau} = g \frac{d}{d\tau} \ln \varphi. \quad (16)$$

In fact, it can also be derived from the sub-Hamiltonian  $F_1 = -g \ln \varphi$ . The evolution equation of  $\tau$  is

$$\frac{d\tau}{ds} = \frac{\partial F}{\partial \Phi} = -\frac{g}{\Phi^2} (H + p_0) + \frac{g}{\Phi} = \frac{g}{\Phi}. \quad (17)$$

Here,  $H + p_0 = 0$  is used. Equation (17) is also given by the sub-Hamiltonian  $F_2 = g \ln \Phi$ . It can give an explicitly analytical solution to the time coordinate:

$$\tau(s) = \tau_0 + s \frac{g}{\Phi}. \quad (18)$$

Combing Equations (16) and (17), we have the relation

$$\frac{d}{d\tau} \ln \Phi = \frac{d}{d\tau} \ln \varphi, \quad (19)$$

<sup>4</sup> $\varphi$  is a function of  $r$  and  $\theta$ , which are functions of  $\tau$ . Thus,  $\varphi$  is also a function that directly depends on  $\tau$ , labeled as  $\varphi = \varphi(r(\tau), \theta(\tau)) = \varphi(\tau)$ .

<sup>5</sup>These solutions also seem to be connected with the second term because  $g$  is a function of  $r$  and  $\theta$ . Here  $r$ ,  $\theta$  and  $\tau$  are regarded as three independent coordinates, as they are in the Hamiltonian  $H$ . However,  $r$  and  $\theta$  are directly related to  $\tau$  in the function  $\varphi$ . In addition,  $\ln(\Phi/\varphi) = 0$  will be shown in a later discussion.

equivalently,

$$\frac{d}{d\tau} \ln \frac{\Phi}{\varphi} = 0, \text{ or } \frac{\Phi}{g} \frac{d}{ds} \ln \frac{\Phi}{\varphi} = 0. \quad (20)$$

Hence,  $\Phi/\varphi$  is constant, i.e.  $\Phi/\varphi = C$ . If  $C = 1$  at the starting time, then we have

$$\Phi/\varphi = 1 \quad (21)$$

for any time  $\tau$  or  $s$ . For simplicity,  $\varphi$  is taken as

$$\varphi = \frac{j}{r}, \quad (22)$$

where  $j$  is still the free parameter in Equation (14).<sup>6</sup> Substituting Equation (22) into Equation (16) yields

$$\frac{d\Phi}{ds} = -\frac{g}{r} \frac{dr}{d\tau}, \quad (23)$$

where  $dr/d\tau = \partial H / \partial p_r = g^{rr} p_r$  is determined by the Hamiltonian (2).  $\Phi$  is analytically solved by

$$\Phi(s) = \Phi_0 - s \frac{g}{r} g^{rr} p_r. \quad (24)$$

This shows that the parameter  $j$  is independent of the integration of  $\Phi$  at time  $s$ , but is only dependent on the initial value  $\Phi_0$ .

The above analyses demonstrate that the Hamiltonian  $F$  is zero for any time  $s$  and consists of  $l + 2$  explicitly integrable terms:

$$F = \frac{1}{\Phi} \sum_{i=1}^l K_i + F_1 + F_2. \quad (25)$$

It is obviously suitable for the application of an adaptive time step explicit symplectic integrator of second order:

$$\begin{aligned} AS_2(h) &= \mathcal{F}_1\left(\frac{h}{2}\right) \times \mathcal{F}_2\left(\frac{h}{2}\right) \times S_2\left(\frac{h}{\Phi}\right) \\ &\quad \times \mathcal{F}_2\left(\frac{h}{2}\right) \times \mathcal{F}_1\left(\frac{h}{2}\right), \end{aligned} \quad (26)$$

where  $\mathcal{F}_1$  and  $\mathcal{F}_2$  respectively correspond to the solvers of the sub-Hamiltonians  $F_1$  and  $F_2$ , and  $h = \Delta s$  is still a fixed step size in the new time variable. In

<sup>6</sup>The simplest choice  $\varphi \propto 1/r$  was considered in the work of Preto & Saha (2009). We guess that  $\varphi = 1/r$ , i.e. Equation (22) with  $j = 1$ , was used. Here,  $j$  is not limited to 1 but has a widely free choice. In later numerical simulations, we shall show what advantage exists for the use of  $j$  in the improvement of integration accuracy and what an appropriate choice of  $j$  is for an individual orbit in every problem.

what follows, several points on the adaptive explicit symplectic scheme are illustrated.

Point 1: The basic clue for the application of the algorithm  $AS_2$  to the Hamiltonian (2) is concluded as follows.

1. Find the desired time transformation function  $g$ .
2. Split the Hamiltonian  $K$  of Equation (6) in the expected form.
3. Write the Hamiltonian  $F$  of adaptive stepsize in Equation (15).
4. Apply a second order explicit symplectic method to solve the Hamiltonian  $F$ .

Point 2: The algorithm  $AS_2$  for  $F$  is implemented as follows.

*Step 1:* Advance  $\Phi$  by  $-ghg^{rr}p_r/(2r)$  in Equation (24).

*Step 2:* Advance  $\tau$  by  $gh/(2\Phi)$  in Equation (18).

*Step 3:* Evolve  $r$ ,  $\theta$ ,  $p_r$  and  $p_\theta$  under  $K$  of Equation (6), using  $S_2$  with the time interval  $h/\Phi$  of Equation (10).

*Step 4:* Reiterate step 2.

*Step 5:* Reiterate step 1.

Point 3: Equations (17), (21) and (22) show that the relation between the two times  $\tau$  and  $s$  is

$$d\tau = g^* ds = \frac{g}{\Phi} ds = \frac{r}{j} g ds, \quad (27)$$

where  $g^*$  is another time transformation function. In practice,  $g^*$  is the time transformation function  $g^*$  of Equation (14). Although  $g^*$  and  $g^*$  are the same time transformation function, the factor  $r/j$  has different contributions to the computations of  $r$ ,  $\theta$ ,  $p_r$  and  $p_\theta$  in the algorithms  $S_2$  and  $AS_2$ . This factor similar to  $g$  typically affects the evolution equations of  $r$ ,  $\theta$ ,  $p_r$  and  $p_\theta$  in the method  $S_2$  with  $g^*$ , and then the computational efficiency is relatively poor. However,  $1/\Phi = r/j$  in Equation (17) is kept constant and only acts as a scaling time factor adjusting the time steps in the computations of  $r$ ,  $\theta$ ,  $p_r$  and  $p_\theta$  by  $S_2(h/\Phi)$  of the algorithm  $AS_2$ . Here,  $\Phi$  remaining constant does not always remain invariant for any time, but in fact it varies with time. It does mean that only when all sub-Hamiltonians  $K_i$  in Equation (15) are solved,  $\Phi$  is regarded as a constant (see Step 3 of Point 2). After a step integration ends,  $\Phi$  is advanced (see Steps 1 and 5 of Point 2). In fact, many numerical experiments in the previous works of Wang et al. (2021a, b, c) and Wu et al. (2021) have confirmed that the integrator  $S_2(h)$  is easy to efficiently implement for the use of the

desired time transformation function  $g$ .<sup>7</sup> In this case,  $S_2(h/\Phi)$  should also efficiently work as  $\Phi$  remains constant. This result reasonably supports that  $AS_2(h)$  should be computationally more efficient. The *efficient implementation* of  $AS_2(h)$  is due to the *constant of  $\Phi$*  in the course of solving all the sub-Hamiltonians  $K_i$ . The function  $g$  ( $\approx 1$  for sufficiently large  $r$ ) in Equation (15) plays a key role in the obtainment of explicitly integrable terms  $K_i$ .

Point 4: The use of different time steps in different parts of an orbit leads to destroying the symplectic property of an integrator that is symplectic for the use of a fixed step size. The fixed time step  $h$  is considered in the new time  $s$ , therefore, the integrator  $AS_2$  remains symplectic. Different time steps appear in different parts of the orbit for the original time  $\tau$ . Smaller old time steps are used for the orbit in the vicinity of the horizon of a black hole, while larger ones are for the orbit far away from the black hole. This fact ensures higher accuracy of the solution at the pericenter or a smaller separation  $r$  and higher efficiency at the apocenter or a larger separation  $r$ . Adaptive time stepping can satisfy the needs. The desired *stretching and shrinking* of the old time steps  $\Delta\tau$  are carried out via the *advancing of  $\Phi$*  after every integration step in the method  $AS_2(h)$ .

Point 5: The adaptive method  $AS_2$  has only additional Steps 1 and 5 in Point 2 as compared with the nonadaptive method  $S_2$ . Therefore, the former method needs a negligibly small amount of cost of additional computation. The desired stretching and shrinking of the step size resulting in the improvement of efficiency of computations for  $AS_2$  is based on both methods achieving the same accuracy of computations. In this case, smaller step sizes are needed.

Point 6: The adaptive time step explicit symplectic integrator  $AS_2$  is not limited to the application of the rotating spacetime (1). In fact, it is suitable for any curved spacetimes, whose corresponding Hamiltonians or time-transformation Hamiltonians exist the desirable splits. A class of spacetimes with direct symplectic analytical integrable decompositions and two sets of spacetimes corresponding to appropriate time-transformation Hamiltonians with the expected splits were introduced by Wu et al. (2022). They allow for the use of  $AS_2$ . Obviously, the efficient implementation of  $S_2$  must lead to that of  $AS_2$ .

<sup>7</sup>No time transformations are needed in the works of Wang et al. (2021a, b, c). In other words,  $g = 1$  is adopt.

In a word, the adaptive time step explicit symplectic method is simple to implement, low at the added cost of computation, and widely applicable to many curved spacetimes.

### 3. Tests and applications of the adaptive method

The adaptive explicit symplectic method  $AS_2$  is applied to integrate three black hole models. In this way, we evaluate its numerical performance by comparing it with the nonadaptive explicit symplectic method  $S_2$ . The dynamical properties of massive test particles or massless photons around some of the black holes are focused on. In numerical tests, the mass of each black hole takes one geometric unit,  $M = 1$ . Dimensionless variables, constants and parameters are also adopted.

#### 3.1. Schwarzschild black hole

A dynamical model of charged particles near the Schwarzschild black hole immersed into an external asymptotically uniform magnetic field was used to test the nonadaptive explicit symplectic method  $S_2$  by Wang et al. (2021a). It is still applied to check the adaptive explicit symplectic method  $AS_2$ . The black hole metric components are

$$\begin{aligned} g_{tt} &= -\left(1 - \frac{2}{r}\right), & g_{rr} &= \left(1 - \frac{2}{r}\right)^{-1}, \\ g_{\theta\theta} &= r^2, & g_{\phi\phi} &= r^2 \sin^2 \theta. \end{aligned} \quad (28)$$

The magnetic field is given by a four-vector electromagnetic potential having only one nonzero covariant component (Wald 1974)

$$A_\phi = \frac{\tilde{B}}{2} r^2 \sin^2 \theta, \quad (29)$$

where  $\tilde{B}$  is the strength of magnetic field. The charged particle motion with charge  $q$  is governed by the Hamiltonian

$$\begin{aligned} H &= \frac{1}{2} g^{\mu\nu} (p_\mu - qA_\mu)(p_\nu - qA_\nu) \\ &= -\frac{1}{2} \left(1 - \frac{2}{r}\right)^{-1} E^2 + \left(L - \frac{\beta}{2} r^2 \sin^2 \theta\right)^2 \\ &\quad / (2r^2 \sin^2 \theta) + \frac{1}{2} \left(1 - \frac{2}{r}\right) p_r^2 + \frac{1}{2} \frac{p_\theta^2}{r^2}, \end{aligned} \quad (30)$$

where  $\beta = q\tilde{B}$ . Take  $r$  as the dimensionless distance and  $r_{pl}$  as the practical distance. Similar notations are given to the other quantities. The dimensionless quantities and the practical ones have their correspondences

as follows:  $r_{pl} = Mr$ ,  $t_{pl} = Mt$ ,  $\tau_{pl} = M\tau$ ,  $E_{pl} = mE$ ,  $q_{pl} = mq$ ,  $p_{r,pl} = mp_r$ ,  $H_{pl} = mH$ ,<sup>8</sup>  $\tilde{B}_{pl} = \tilde{B}/M$ ,  $L_{pl} = MmL$  and  $p_{\theta,pl} = Mmp_\theta$ . Here,  $m$  is the mass of the charged particle. Wang et al. (2021a) pointed out that this Hamiltonian *does not need any time transformation and can directly be split into four explicitly analytical solvable parts*. The related quantities in Equations (6) and (7) correspond to

$$p_0 = \frac{1}{2}, \quad g(r, \theta) = 1, \quad (31)$$

$$\begin{aligned} K_1 &= f(r, \theta) + p_0 \\ &= -\frac{1}{2} \left(1 - \frac{2}{r}\right)^{-1} E^2 + \left(L - \frac{\beta}{2} r^2 \sin^2 \theta\right)^2 \\ &\quad / (2r^2 \sin^2 \theta) + \frac{1}{2}, \end{aligned} \quad (32)$$

$$K_2 = \frac{1}{2} p_r^2, \quad (33)$$

$$K_3 = -\frac{1}{r} p_r^2, \quad (34)$$

$$K_4 = \frac{p_\theta^2}{2r^2}. \quad (35)$$

Hence, the methods  $S_2$  and  $AS_2$  can work.

The particle's energy  $E = 0.995$  and the angular momentum  $L = 4$  are chosen. The new time step  $h = 1$  and the free parameter  $j = 100$  in Equation (22) are used. Two cases without magnetic field  $\beta = 0$  and with magnetic field  $\beta = 9.7 \times 10^{-4}$  are considered in the Schwarzschild spacetime. An orbit with initial conditions  $r = 7$ ,  $\theta = \pi/2$ ,  $p_r = 0$  and  $p_\theta > 0$  solved from the equation  $H + p_0 = 0$  is tested. Figure 1a plots the phase space structures of  $r$  and  $p_r$  of this orbit in the two cases via Poincaré section at the plane  $\theta = \pi/2$  with  $p_\theta > 0$ . The two algorithms  $S_2$  and  $AS_2$  are almost the same in the obtained structures. In the case of  $\beta = 0$ , the Schwarzschild spacetime is integrable and does not allow for the presence of chaos. A regular Kolmogorov-Arnold-Moser (KAM) torus on the Poincaré section is what we expect. For  $\beta = 9.7 \times 10^{-4}$ , the Hamiltonian system (30) is non-integrable and possibly chaotic. Many discrete points distributed in a area on the Poincaré section indicate the characteristic of chaos. The chaotic behavior was also shown by Pánis et al. (2019) using the time series analysis method. Clearly, the distance with  $r_{max} \approx 150$  for  $\beta = 9.7 \times 10^{-4}$  is smaller than that with  $r_{max} \approx 190$  for  $\beta = 0$ . That is, the existence of magnetic field leads

<sup>8</sup>If  $H = g^{\mu\nu} (p_\mu - qA_\mu)(p_\nu - qA_\nu)/(2m)$ , then  $H_{pl} = mH$ . However,  $H_{pl} = m^2 H$  if  $H = g^{\mu\nu} (p_\mu - qA_\mu)(p_\nu - qA_\nu)/2$ .



to decreasing the motion region of charged particles, as compared with the absence of magnetic field.

For the two values of magnetic parameter  $\beta$  in Figure 1b, the methods  $AS_2$  and  $S_2$  give no secular growth to the errors of the Hamiltonian,  $\Delta H = H + p_0$ . Such good long-term stability and error behavior share some of the benefits of the standard symplectic integrators with constant time steps. The errors in the order of  $10^{-7}$  for  $AS_2$  are two orders of magnitude smaller than those in the order of  $10^{-5}$  for  $S_2$ . This shows that the use of variable steps is favorable for the accuracy of computations, as compared with that of constant steps. In addition, the regular dynamics for  $\beta = 0$  and the chaotic dynamics for  $\beta = 9.7 \times 10^{-4}$  have no significant differences in the Hamiltonian errors for each of the two algorithms.

Seen from the relation between the proper time  $\tau$  and the new time  $s$  for the method  $AS_2$  in Figure 1c, the proper time  $\tau$  is about  $9.7 \times 10^3$  for the regular case of  $\beta = 0$ , and about  $8.1 \times 10^3$  for the chaotic case of  $\beta = 9.7 \times 10^{-4}$  when  $s = 10^4$ . Namely,  $\tau$  and  $s$  are nearly consistent for the former case, and are somewhat different for the latter case.

Although the approximate equivalence of  $\tau$  and  $s$  is present in the method  $AS_2$  for  $\beta = 0$ ,  $AS_2$  still exhibits better accuracy in the integrals of motion than  $S_2$ . This is attributed to the application of the desired stretching and shrinking of the proper time steps  $\Delta\tau$  to  $AS_2$ .  $\Delta\tau$  grows nearly linearly with the distance  $r$  in Figure 1d. Different step sizes appear in different values of  $r$  during integration of the orbit. The step size is smaller for a shorter distance  $r$ , whereas larger for a longer distance  $r$ . This treatment of the step sizes is useful to significantly improve accuracy and efficiency of computations.

The accuracy of the method  $AS_2$  relies on different choices of  $j$  in Equation (22). The accuracy of integrations is improved typically as  $j$  increases in Table 1. The difference between  $\tau$  and  $s$  gets larger, too. To make the difference as small as possible, we roughly take  $j \sim (r_{min} + r_{max})/2$ , where  $r_{min}$  is the smallest distance of the bounded orbit. Based on better accuracy and extremely smaller difference between  $\tau$  and  $s$ ,  $j = 100$  is perhaps a better choice in the present situation.

We have demonstrated in detail an efficient implementation of the adaptive time step explicit symplectic integration algorithm to the Schwarzschild spacetime. The implementation is relatively easy be-

cause this spacetime has its Hamiltonian system that can be directly split into several explicitly integrable terms without time transformation (i.e.  $g = 1$ ). There are many other black hole spacetimes satisfying this property. In fact, the known spacetimes, including Reissner-Nordström black hole (Wang et al. 2021b), Reissner-Nordström-(anti)-de Sitter black hole (Wang et al. 2021c), modified gravity Schwarzschild black hole (Yang et al. 2022), rotating black ring (Wu et al. 2022), Brane-world metric (Hu & Huang 2022), Einstein-Æther black hole (Liu & Wu 2023), Konoplya-Zhidenko black hole (He et al. 2023), and Horndeski gravity hairy black hole (Cao et al. 2024), have been given the desired splitting forms. Without doubt, our adaptive time step explicit symplectic scheme should also be well suited for studies of these spacetimes.

### 3.2. Kerr black hole

The Kerr spacetime describes a rotating black hole geometry, which has covariant nonzero components (Kerr 1963):

$$\begin{aligned} g_{tt} &= -\left(1 - \frac{2r}{\Sigma}\right), & g_{t\phi} &= -\frac{2ar\sin^2\theta}{\Sigma} = g_{\phi t}, \\ g_{rr} &= \frac{\Sigma}{\Delta}, & g_{\theta\theta} &= \Sigma, \\ g_{\phi\phi} &= \left(\rho^2 + \frac{2ra^2}{\Sigma}\sin^2\theta\right)\sin^2\theta, \end{aligned} \quad (36)$$

which  $\Delta = \rho^2 - 2r$  and  $\rho^2 = r^2 + a^2$ . The dimensionless spin parameter  $a$  corresponds to its practical spin  $a_{pl} = aM$ . For the Kerr geometry, the Hamiltonian (2) cannot be directly split into more than two explicitly integrable parts because  $\Sigma$  acts as the denominators of the second, third terms of Equation (2). However, Wu et al. (2021) can still split the time-transformed Hamiltonian (6) into five explicit analytical solvable terms using the time transformation function  $g$  of Equation (11) to eliminate the factor  $\Sigma$  of the denominators. This brings a good chance for the application of the method  $S_2$ . Naturally, the method  $AS_2$  is easily available, too.

#### 3.2.1. Time-like geodesics

For the time-like geodesic motion of a massive test particle around the Kerr black hole, we take  $p_0 = 1/2$  in Equations (6) and (15). Suppose that the black hole spin parameter is  $a = 0.8$ , and the particle has its energy  $E = 0.995$  and angular momentum  $L = 4.6$ . The new time step  $\Delta s = h = 1$  and  $j = 100$  are still used.

An orbit with its initial conditions of  $r = 9.8$ ,  $p_r = 0$  and  $\theta = \pi/2$  is chosen as a tested orbit. It is regular because of the integrability of the Kerr spacetime.

The accuracy in the Hamiltonian  $K$  of Equation (6) is two orders of magnitude better for  $AS_2$  than for  $S_2$ , as shown in Figure 2a. However, the proper time  $\tau$  for  $S_2$  or  $AS_2$  arrives at 10,000 when the time  $w$  or  $s$  reaches 10,000. That is,  $\tau \approx w$  for  $S_2$  and  $\tau \approx s$  for  $AS_2$ . Of course, there are some differences between them in Figure 2b.  $\tau$  increases linearly with time  $w$  for  $S_2$ , whereas it does nonlinearly with time  $s$  for  $AS_2$ .  $j = 100$  for  $AS_2$  is again demonstrated to be an appropriate choice adjusting the relation between  $\tau$  and  $s$  as the smallest difference. In spite of no typical differences between the proper time  $\tau$  and the transformation time  $w$  or  $s$  in the two methods, the proper time step  $\Delta\tau$  of  $S_2$  almost remains constant, while that of  $AS_2$  is variable in Figure 3c. The constant step size of  $S_2$  is adopted due to the time transformation function  $g \approx 1$  of Equation (11) for sufficiently large distance  $r$ . The adaptive time steps of  $AS_2$  are employed because of  $\Phi$  in the time transformation function  $g^* = g/\Phi \approx 1/\Phi$  of Equation (27) being varied according to Equation (24). The use of adaptive time steps makes a crucial contribution to the accuracy of  $AS_2$  superior to that of  $S_2$ . In addition to the dependence of the proper time steps  $\Delta\tau$  on the distances  $r$  seen from Figure 3c, the integrated orbit is bounded because its distances  $r$  have the maximum value and the minimum value.

### 3.2.2. Null geodesics

For the null geodesic dynamics of massless photons near the Kerr black hole, we take  $p_0 = 0$  in Equations (6) and (15). Unlike the orbits of particles, all orbits of photons are unstable except some particular regions. For example, the black hole regime  $0 < r < r_{h^-}$  within the inner horizon  $h^- = 1 - \sqrt{1 - a^2}$  ( $|a| < 1$ ) allows the existence of stable equatorial circular photon orbits (Dolan & Shipley 2016). Photon orbits outer the horizons of the Kerr black hole belong to one of the three regions: falling to the center, scattering to infinity and unstably circling in the center (Bardeen & Cunningham 1973).

Consider that a photon orbit scattering to infinity corresponds to the parameters  $a = 0.3$ ,  $E = 0.99$ ,  $L = 3\sqrt{3}E/10$  and the initial conditions  $r = 3$ ,  $\theta = \pi/2$ ,  $p_r = 0$ . Taking  $h = 0.1$  and  $j = 1000$ , we integrate this escaping orbit until the distance increases to  $r = 1000$ .

Although the two methods  $S_2$  and  $AS_2$  almost run the same original time  $\tau \approx 1,016$ , they use different new times:  $s = 1,016$  for  $S_2$  and  $s = 8,103$  for  $AS_2$ . Because of this point, the curves  $\tau$ - $K$  for two algorithms are plotted in Figure 3a instead of the curves  $w$  ( $s$ )- $K$  in Figure 2a. The errors in the Hamiltonian  $K$  still remain stable. They are about two orders of magnitude larger for  $S_2$  than for  $AS_2$ . In Figure 3b, the old step sizes are basically constant for  $S_2$  but grow linearly with the distances  $r$  for  $AS_2$ . Different values of  $j$  in the method  $AS_2$  affect the accuracies of  $K$  and the values of new time  $s$ . Seen from Table 2,  $j = 1000$  is perhaps the best choice.

What about the performance of the method  $AS_2$  when this scattering orbit is replaced with an orbit falling to the black hole? To answer this question, we choose the parameters  $a = 0.5$ ,  $E = 0.996$ ,  $L = -2.211$  and the initial conditions  $r = 100$ ,  $\theta = \pi/2$ ,  $p_r = -1.016$ .  $h = 0.001$  is used, and several values are also given to  $j$  in the integrator  $AS_2$ . The integrations have to end when the distance  $r$  decreases to 2 at the nearby horizon of the black hole. Figure 4a shows that the increase of  $j$  does not necessarily lead to good results, and  $j = 100$  should be the best choice. The symplectic integrators yield drifts in the errors  $K$  when the orbit approaches the horizon.  $AS_2$  with  $j = 100$  can perform better accuracy in the vicinity of the horizon than  $S_2$ . This advantage is helpful to apply  $AS_2$  to a new ray-tracing method to obtain black hole images by finding the related photon regions in the observer's plane. Both the fixed time step of  $S_2$  and the adaptive time steps of  $AS_2$  are displayed clearly in Figure 4b.

In short, the simulations of the motions of particles and photons around the Kerr black hole show that the efficient implementation of  $AS_2$  has two keys. One key is the obtainment of the desired time transformation functions  $g$ .  $g$  should make the related time-transformed Hamiltonians have explicitly integrable splits, and should be approximately equal to 1 or some constants. Such functions can be found in some other literature besides the works of Wu et al. (2021), Sun et al. (2021a, b) and Wu et al. (2022) on the Kerr type spacetimes. They exist in non-Schwarzschild black holes in modified theories of gravity (Zhang et al. 2021), regular charged black hole (Zhang et al. 2022), Reissner-Nordström-Melvin black hole (Hu & Huang 2023; Yang et al. 2023), Kerr-Newman-Melvin black hole (Yang & Wu 2023) and renormalized group improved Schwarzschild black hole (Lu & Wu 2024). In addition to these examples, the desired time transfor-

mation functions  $g$  in several black hole spacetimes are listed in Appendix A. It is also easy to find such similar time transformation functions  $g$  when the method  $AS_2$  is applied to simulate the chaotic dynamics of particle orbits around Kerr black holes surrounded by external magnetic fields (Takahashi & Koyama 2009; Stuchlík & M. Kološ 2016; Tursunov et al. 2016; Kopáček & Karas 2018; Tursunov et al. 2020; Kološ et al. 2021). The other key is an appropriate choice of  $j$ . In general,  $j$  is roughly given in the range of  $(r_{min} + r_{max})/2 \leq j \leq r_{max}$ . In particular, it would be good to choose  $j$  as the observer's distance in ray-tracing integrations.

### 3.3. Schwarzschild-Melvin black hole

Ernst (1976) gave a Schwarzschild-Melvin black hole describing the Schwarzschild black hole immersed in the magnetic universe of Melvin (1965). This black hole is an exact solution of Einstein's equations. Besides the solution, the Reissner-Nordström-Melvin black hole and Kerr-Newman-Melvin black hole were presented. The Schwarzschild-Melvin black hole has nonzero metric components

$$\begin{aligned} g_{tt} &= -\Lambda^2 \left(1 - \frac{2}{r}\right), & g_{rr} &= \Lambda^2 \left(1 - \frac{2}{r}\right)^{-1}, \\ g_{\theta\theta} &= \Lambda^2 r^2, & g_{\phi\phi} &= \Lambda^{-2} r^2 \sin^2 \theta, \end{aligned} \quad (37)$$

where function  $\Lambda$  is given by

$$\Lambda = 1 + \frac{1}{4} B^2 r^2 \sin^2 \theta. \quad (38)$$

The dimensionless magnetic field  $B$  corresponds to the practical one  $B_{pl} = B/M$ .

If the magnetic field vanishes, this spacetime is the Schwarzschild black hole. When it is nonzero, it acts as a gravitational effect, which causes this spacetime not to be asymptotically flat. If  $|B| \ll 1$  and  $2 \ll r \ll 1/B$ , then  $\Lambda \approx 1$  outside the horizon. This means the existence of the approximately flat spacetime and the approximately uniform magnetic field. In this case, this spacetime is *nearly integrable*. This fact was confirmed by finding chaos of neutral particles around the Schwarzschild-Melvin black hole in the works of Karas & Vokrouhlický (1992) and Li & Wu (2019). Of course, neutral particles can also be chaotic in the Reissner-Nordström-Melvin black hole spacetime (Yang et al. 2023) and Kerr-Newman-Melvin black hole spacetime (Yang & Wu 2023). On the other

hand, self-similar fractal structures appear in the shadows of the Schwarzschild-Melvin black hole (Junior et al. 2021) and Kerr-Melvin black hole (Wang et al. 2021; Hou et al. 2022). The chaotic lensing, i.e. the chaotic motion of photons, is responsible for these self-similar fractal structures in the black hole shadows.

We select the time transformation function of Equation (5) as

$$g = \Lambda^2. \quad (39)$$

The time-transformed Hamiltonian  $K$  of Equation (6) resembles the Hamiltonian  $H$  of Schwarzschild black hole in Equation (30) with  $\beta = 0$ . That is, it consists of four explicitly integrable terms. In fact, only Equation (32) in Equations (32)-(35) is slightly modified as

$$K_1 = -\frac{rE^2}{2(r-2)} + \frac{L^2\Lambda^4}{2r^2\sin^2\theta} + p_0\Lambda^2. \quad (40)$$

Although  $E$  and  $L$  are usually called as the energy and angular momentum of the photon in the Schwarzschild-Melvin spacetime, they are unlike those in the Kerr metric. For the former spacetime,  $E$  is not the particle's or photon's energy measured by an observer at spatial infinity unless the observer lies on the axis of symmetry (Junior et al. 2021). However,  $E$  is always the energy measured at spatial infinity for the latter spacetime. It is clear that the methods  $AS_2$  and  $S_2$  are suitably applicable to the time-transformed Hamiltonian  $K$  of the Schwarzschild-Melvin black hole spacetime.

#### 3.3.1. Dynamics of massive test particles

For the motion of a massive neutral test particle around the black hole, the parameters are given by  $E = 0.9905$ ,  $L = 3.6$  and  $B = 0.001$ . The step size  $h = 1$  and the parameter  $j = 100$  are also given. In Figure 5a,  $g \approx 1$  outside the horizon can be guaranteed obviously. The method  $S_2$  seems to show the regularity of Orbit 1 with the initial separation  $r = 10$ . However, the method  $AS_2$  describes that the orbit allows the onset of chaos confined to very narrow bands in this section. The result is consistent with that of Figure 4b in the work of Li & Wu (2019). The chaoticity of such a neutral particle is due to the magnetic field in Equation (38) acting as a gravitational effect in the spacetime geometry. Notice that the magnetic fields in Equations (29) and (38) have different contributions. The magnetic field in Equation (29) does not affect the

spacetime background (28) but the motion of charged particles in Equation (30). Namely, the spacetime (28) is still integrable, but the Hamiltonian (30) is not. Nevertheless, the magnetic field in Equation (38) directly changes the spacetime background (37) and makes it nonintegrable. Naturally, it affects the motion of particles. In this sense, the occurrence of chaos is possible. Both methods almost give the same dynamical information to any one of Orbits 2-6. In particular, Orbit 5 with the initial separation  $r = 48.7$  has a saddle point with one stable direction and another unstable direction.

Both algorithms showing different results on the dynamics of Orbit 1 is because  $AS_2$  provides two orders of magnitude better accuracy than  $S_2$  in Figure 5b. When the integration adds up to 10,000 steps, the proper time  $\tau$  is approximately equal to the time  $w$  for  $S_2$ , and about half the time  $s$  for  $AS_2$  in Figure 5c. The nearly constant step size  $\Delta\tau$  is used for  $S_2$ , while the variable step sizes  $\Delta\tau$  are for  $AS_2$  in Figure 5d.

The method  $AS_2$  is used to explore the transition from order to chaos as the magnetic field strength  $B$  is varied. When the magnetic field strength is slightly smaller than that in Figure 5, all orbits in Figure 5a become regular for  $B = 0.8 \times 10^{-3}$  in Figure 6a. The shapes of Orbits 2-6 are unlike those in Figure 5a. A saddle point exists for Orbit 5 in Figure 5a, but does not exist in Figure 6a. As the magnetic field strength is slightly larger than that in Figure 5, chaos of Orbit 1 in Figure 5 dies out for  $B = 1.2 \times 10^{-3}$  in Figure 6b. Orbit 5 and orbit 7 with the initial distance  $r = 45$  become chaotic in the present case. The chaotic region in Figure 6b is larger than in Figure 5a.

It can be seen from Figures 5 and 6 that an increase of the magnetic field strength enhances the extent of chaos of massive neutral test particles. Strengthening the extent of chaos is considered from a statistical result of the global phase space rather than one single orbit.

### 3.3.2. Dynamics of massless photons

Now, we use the method  $AS_2$  with the step size  $h = 1$  to simulate the motion of a photon near the Schwarzschild-Melvin black hole. The parameters are  $E = 0.995$ ,  $B = 0.1$  and  $j = 100$ . Consider that an orbit has its initial radius  $r = 15$ . The angular momentum is governed by  $L = -E\sqrt{-g_{\phi\phi}/g_{tt}}$ .<sup>9</sup> This orbit is

chaotically filled in a great region of Figure 7a. When the parameters  $E$  and  $L$  are given, a slight decrease of the magnetic field strength  $B$  causes the transition from chaos to order. The chaotic regions become gradually small and the number of regular KAM tori increases for the magnetic field strength varied from  $B = 0.095$  in Figure 7b to  $B = 0.091$  in Figure 7c and  $B = 0.088$  in Figure 7d. When  $B = 0.086$  in Figure 7e and  $B = 0.084$  in Figure 7f, chaos is absent and all orbits are regular KAM tori.

In fact, Figure 7 shows the existence of stable bound regular photon orbits and stable bound chaotic photon orbits, which neither fall into the black hole nor escape to infinity. This figure is similar to Figures 5 and 6 for the description of stable bound regular particle orbits and stable bound chaotic particle orbits existing in the Schwarzschild-Melvin spacetime. It is unlike Figures 3 and 4, where no stable bound photon orbits but falling photon orbits and escaping ones exist outside the horizon in the Kerr spacetime. These results are easily shown via effective potentials on the equatorial plane. The photon effective potential similar to the particle one for the Schwarzschild-Melvin spacetime has closed pockets corresponding to minimum values (Junior et al. 2021). The presence of such closed pockets allows that of stable bound photon orbits on (or outside) the equatorial plane in the Schwarzschild-Melvin spacetime. In a similar way, stable light rings could exist in the Kerr-Melvin spacetime (Wang et al. 2021d). There are also stable light rings and chaotic lensing of light near rotating boson stars and Kerr black holes with scalar hair (Cunha et al. 2015, 2016). Stable regular or chaotic photon orbits were found in stationary axisymmetric electrovacuum (Dolan & Shipley 2016). However, the absence of closed pockets in the photon effective potential does not allow for the existence of stable bound photon orbits outside the horizon of the Kerr spacetime.

Comparing between Figure 7 and Figures 5, 6, one clearly finds that the stable bound photon orbits can exist for larger magnetic fields in the Schwarzschild-Melvin spacetime, but the stable bound particle orbits can for smaller magnetic fields. These results are also seen from the effective potentials on the equatorial plane. Wang et al. (2021d) showed that the radii of stable light rings decrease with the magnetic field parameter  $B$  increasing in the Kerr-Melvin spacetime. For the Kerr spacetime with  $B = 0$ , the stable light ring

<sup>9</sup>The choice of  $L$  is based on the impact parameter  $\eta = L/E$  for the effective potential vanishing at the equatorial plane. Here, the potential is nonzero for the initial radius  $r = 15$ .

<sup>9</sup>The choice of  $L$  is based on the impact parameter  $\eta = L/E$  for the effective potential vanishing at the equatorial plane. Here, the po-

radius tends to infinity. This point means that no stable light rings exist outside the horizon in the Kerr spacetime. The effective potentials for the Schwarzschild-Melvin spacetime are also similar to those for the Kerr-Melvin spacetime. The stable particle circular orbits can be allowed for smaller magnetic fields, whereas the smaller radii of stable light rings can for larger magnetic field parameters  $B$ . The smaller radii of stable light rings mean the shapes of the effective potentials going towards the black hole and an increase of the gravitational effects. This result leads to enlarging the motion regions of stable bound photon orbits and strengthening the extent of chaos outside the equatorial plane for larger magnetic field strengths in the Schwarzschild-Melvin spacetime.

Because a larger value of the magnetic field strength  $B$  can easily allow the presence of stable bound orbits outside the equatorial plane in the Schwarzschild-Melvin spacetime,  $\Lambda \approx 1$  is no longer present. In fact, the range of  $\Lambda$  in Figure 7a is  $1 < \Lambda < 1.6$ , which is different from  $\Lambda \approx 1$  in Figures 5 and 6. It is clearly shown in Figure 8a that the range of  $g$  is  $1.2 < g < 2.5$ . In other words, the old time steps  $\Delta\tau$  for the method  $S_2$  roughly use variable step sizes in the range of  $1.2 < \Delta\tau < 2.5$ . The old time steps for the method  $AS_2$  are adjusted according to the variation of  $r$  from 0.1 to 1.1. The old time steps  $\Delta\tau$  do not grow linearly with the separation  $r$  for both methods. In this case, the differences between the old times  $\tau$  and the time-transformed times  $w$  or  $s$  should be large in Figure 8b. After  $10^5$  integration steps, the old times are  $\tau = 1.8 \times 10^5$  for  $S_2$ , and  $\tau = 3 \times 10^4$  for  $AS_2$ . The error in the Hamiltonian  $K$  is about two orders of magnitude smaller for  $AS_2$  than for  $S_2$ , as shown in Figure 8c. When the chaotic orbit in Figure 7a is replaced with the regular orbit with the initial distance  $r = 15$  in Figure 7b, the Hamiltonian errors between the two cases have no explicit differences for each of the two algorithms.

#### 4. Summary

Some curved spacetimes, which are directly split into several explicitly integrable parts, are easily fit for the application of explicit symplectic integrators, as was introduced in the previous papers (Wang et al. 2021a, b, c). Some other curved spacetimes, which are not directly split into several explicitly integrable parts but are through appropriate time transformations, can also allow for the construction of explicit symplectic

methods, as was reported in the previous works (Wu et al. 2021, 2022). Adaptive time steps should be admitted in such time-transformed explicit symplectic methods from the theoretical viewpoint. However, they are rather cumbersome to implement in general from practical computations. The time transformation functions for the efficient implementation of time-transformed explicit symplectic algorithms should satisfy the time-transformed Hamiltonians having explicitly integrable splits, and should approach 1 or some constants<sup>10</sup> for sufficiently large radial distances.

Combing the desired time transformation functions and the step-size control technique proposed by Preto & Saha (2009), we have developed an adaptive time step explicit symplectic integrator for many curved spacetimes. Besides an appropriate choice of the time transformation function, another key for the efficient implementation of such an adaptive time step explicit method is the introduction of a conjugate momentum  $\Phi$  with respect to the old time as an additional coordinate. Here  $\Phi$  acts as a rescaled time variable adjusting the time steps in integrations. The constant of  $\Phi$  in the course of solving the other momenta and coordinates brings the efficient implementation and good computational efficiency of the proposed algorithm. The advancing of  $\Phi$  after every integration step leads to the desired stretching and shrinking of the old time steps in the method. A suitable choice of the parameter  $j$  is also necessary. The adaptive method has only two additional steps as compared with the nonadaptive one. The efficient implementation of the latter method naturally results in that of the former one. Therefore, the adaptive method needs a negligibly small amount of cost of additional computation, and its implementation is simple.

We have shown that the new adaptive time step explicit symplectic integrator works well for numerical studies of several dynamical problems. These problems include the motion of particles around the Schwarzschild black hole immersed in an external magnetic field, the dynamics of particles and photons near the Kerr black hole, and the motion of particles and photons around the Schwarzschild-Melvin black hole. The numerical tests have demonstrated that the adaptive method typically improves the efficiency of the nonadaptive method. Even if the origi-

<sup>10</sup>This requirement is considered in the generic case. There are exceptional cases, e.g. the choice of time transformation function for the motion of photons around the Schwarzschild-Melvin black hole.

nal time and the newly transformed time have no explicit differences (see e.g. Figures 1c, 2b and Tables 1, 2), the desired stretching and shrinking of the step-size still show good performance in the suppression of long-term qualitative errors. Because of such desirable property, the new adaptive method is applied to investigate dependence of the transition from order to chaos on a small change of the magnetic field strength. It is found that stable bound photon orbits involving regular orbits and chaotic ones, which neither spiral toward into the black hole nor spiral out to infinity, can exist outside the horizon in the Schwarzschild-Melvin spacetime, but cannot in the Kerr spacetime. In addition, the chaotic regions are enlarged with an increase of the magnetic field strength for either the motion of particles or the motion of photons around the Schwarzschild-Melvin black hole.

The adaptive time step explicit symplectic method is suitable for integrations of highly eccentric orbits and close encounters in the Solar System. In addition, it can be applied to many curved spacetimes ranging from the problems considered in the present paper, the spacetimes motioned in Appendix A and the literature (e.g. Wang et al. 2021a; Wu et al. 2021, 2022; Yang & Wu 2023; Cao et al. 2024), and some other spacetimes such as scalar fields (Virbhadra et al. 1998), black-bounce-Reissner-Nordström spacetime (Zhang & Xie 2022) and quantum gravity Schwarzschild black holes (Gao & Deng 2021; Huang & Deng 2024). It is useful to simulate the motion of particles and photons outside the black hole horizons in the phase space. In particular, it is suitable for integrations of particles and photons in the vicinity of the black hole horizons. It is also applicable to backwards ray-tracing methods, which study the light rays from points in an observer's local sky how to correspond to the final evolution of photon orbits in the phase space and obtain shadows of black holes. An appropriate choice of the parameter  $j$  of Equation (22) would be the observer's distance in the ray-tracing integrations.

## A. Suitable choices of time transformation functions $g$ in several black hole spacetimes

Four black hole spacetimes are given, and the related time transformation functions are also provided.

### A.1. Einstein-Maxwell-Dilaton-Axion metric

The Einstein-Maxwell-Dilaton-Axion metric describes a static, axisymmetric rotating black hole, as a non-general relativity black hole solution coupling metric parameters to a physical field. García et al. (1995) gave the metric components:

$$\begin{aligned} g_{tt} &= -\left(\frac{\hat{\Delta} - a^2 \sin^2 \theta}{\hat{\Sigma}}\right), & g_{t\phi} &= -\frac{a(\delta - W\hat{\Delta}) \sin^2 \theta}{\hat{\Sigma}}, \\ g_{rr} &= \frac{\hat{\Sigma}}{\hat{\Delta}}, & g_{\theta\theta} &= \hat{\Sigma}, & g_{\phi\phi} &= \frac{\hat{A}}{\hat{\Sigma}} \sin^2 \theta, \end{aligned} \quad (\text{A1})$$

where the related notations are expressed as

$$W = 1 + [\beta_{ab}(2 \cos \theta - \beta_{ab}) + \beta_a^2] \csc^2 \theta, \quad (\text{A2})$$

$$\hat{\Sigma} = \Sigma - (\beta^2 + 2br) + \beta_b(\beta_b - 2a \cos \theta), \quad (\text{A3})$$

$$\hat{\Delta} = \Delta - (\beta^2 + 2br) + (1 + 2b)\beta_b^2, \quad (\text{A4})$$

$$\hat{A} = \delta^2 - a^2 \hat{\Delta} W^2 \sin^2 \theta, \quad (\text{A5})$$

$$\delta = r^2 - 2br + a^2. \quad (\text{A6})$$

$b$  and  $\beta$  with units of length are the coupling parameters of the dilaton and axion fields.  $\beta_a$ ,  $\beta_{ab}$  and  $\beta_b$  are dimensionless parameters. This metric is also found in the paper of Younsi et al. (2023).

Noting Equation (2), we obtain

$$g^{rr} = \frac{\hat{\Delta}}{\hat{\Sigma}}, \quad g^{\theta\theta} = \frac{1}{\hat{\Sigma}}. \quad (\text{A7})$$

When the time transformation function of Equation (5) is taken as

$$g = \frac{\hat{\Sigma}}{r^2}, \quad (\text{A8})$$

the Hamiltonian (6) is made of explicitly solvable five terms, and  $g \rightarrow 1$  for  $r \rightarrow \infty$ .

### A.2. Charged Horndeski black hole

An asymptotically flat solution describing a charged Horndeski black hole is shown in the paper of Cisterna & Erices (2014) as follows:

$$\begin{aligned} g_{tt} &= -\left(1 - \frac{2}{r} + \frac{4Q^2}{r^2} - \frac{4Q^4}{3r^4}\right), & g_{\theta\theta} &= r^2, \\ g_{rr} &= -\frac{(8r^2 - 16Q^2)^2}{64r^4 g_{tt}}, & g_{\phi\phi} &= r^2 \sin^2 \theta, \end{aligned} \quad (\text{A9})$$

where  $Q$  is the electric charge parameter of black hole. Letting the time transformation function be

$$g = -\frac{(8r^2 - 16Q^2)^2}{64r^4 g_{tt}}, \quad (\text{A10})$$

we obtain  $g \rightarrow 1$  for  $r \rightarrow \infty$  and can split the Hamiltonian (6) into several explicitly solvable pieces.

### A.3. Hairy Kerr black hole

A stationary and axisymmetric hairy Kerr black hole is given by Contreras et al. (2021) in the form

$$\begin{aligned} g_{tt} &= -\frac{\check{\Delta} - a^2 \sin^2 \theta}{\Sigma}, & g_{t\phi} &= -a \left( 1 - \frac{\check{\Delta} - a^2 \sin^2 \theta}{\Sigma} \right) \sin^2 \theta, \\ g_{rr} &= \frac{\Sigma}{\check{\Delta}}, & g_{\theta\theta} &= \Sigma, & g_{\phi\phi} &= \sin^2 \theta \left( \Sigma + a^2 \sin^2 \theta \left( 2 - \frac{\check{\Delta} - a^2 \sin^2 \theta}{\Sigma} \right) \right), \end{aligned} \quad (\text{A11})$$

where

$$\check{\Delta} = r^2 + a^2 - 2r + \xi r^2 e^{-r/(1-l_0/2)}. \quad (\text{A12})$$

Here  $\xi$  is a deviation parameter, and  $l_0$  is a primary hair parameter. If the time transformation function is chosen as

$$g = \frac{\Sigma}{\check{\Delta}}, \quad (\text{A13})$$

then  $g \rightarrow 1$  for sufficiently large distance  $r$  and the Hamiltonian (6) has the desired split.

### A.4. Loop quantum gravity rotating black hole

Islam et al. (2023) investigated Event Horizon Telescope observations of the effects of a rotating black hole solution in loop quantum gravity (Kumar et al. 2022). This solution is described by

$$\begin{aligned} g_{tt} &= -\left( 1 - \frac{2\bar{M}}{\bar{\rho}^2} \sqrt{r^2 + l^2} \right), & g_{t\phi} &= -2a\bar{M} \sqrt{r^2 + l^2} \sin^2 \theta, \\ g_{rr} &= \frac{\bar{\rho}^2}{\bar{\Delta}}, & g_{\theta\theta} &= \bar{\rho}^2, & g_{\phi\phi} &= \frac{\bar{A}}{\bar{\rho}^2} \sin^2 \theta, \end{aligned} \quad (\text{A14})$$

where

$$\bar{M} = 1 - \frac{1}{2} \left( r - \sqrt{r^2 + l^2} \right), \quad (\text{A15})$$

$$\bar{\rho}^2 = r^2 + l^2 + a^2 \cos^2 \theta, \quad (\text{A16})$$

$$\bar{\Delta} = r^2 + l^2 + a^2 - 2\bar{M} \sqrt{r^2 + l^2}, \quad (\text{A17})$$

$$\bar{A} = (r^2 + l^2 + a^2)^2 - a^2 \bar{\Delta} \sin^2 \theta. \quad (\text{A18})$$

Here  $l$  is the bounce radius. We select the time transformation function as

$$g = \frac{\bar{\rho}^2}{\bar{\Delta}}. \quad (\text{A19})$$

Obviously,  $g \rightarrow 1$  for sufficiently large distance  $r$ . Thus, the Hamiltonian (6) can be separated into explicitly solvable several parts.

### Acknowledgments

The authors are very grateful to a referee for valuable comments and suggestions. This research has been supported by the National Natural Science Foundation of China [Grant Nos. 11973020, 12073008 and 12473074].



## REFERENCES

- Bacchini, F., Ripperda, B., Chen, A. Y., & Sironi, L. 2018, *ApJS*, 237, 6
- Bacchini, F., Ripperda, B., Chen, A. Y., & Sironi, L. 2019, *ApJS*, 240, 40
- Bardeen, C. T., & Cunningham, J. M. 1973, *ApJ*, 183, 237
- Blanes, S., Casas, F., & Escorihuela-Tomàs, A. 2024, *Appl. Numer. Math.* 204, 86
- Blanes, S., Casas, F., & Murua, A. 2008, *Bol. Soc. Esp. Math. Apl.*, 45, 89
- Blanes, S., Casas, F., & Murua, A. 2010, *Bol. Soc. Esp. Math. Apl.*, 50, 47
- Blanes, S., & Moan, P. C. 2002, *JCoAM*, 142, 313
- Brown, J. D. 2006, *PhRvD*, 73, 024001
- Cao, W., Wu, X., & Lyv, J. 2024, *Eur. Phys. J. C*, 84, 435
- Cisterna, A., & Erices, C. 2014, *PhRvD*, 89, 084038
- Contreras, E., Ovalle, J., & Casadio, R. 2021, *PhRvD*, 103, 044020
- Cunha, P. V. P., Herdeiro, C. A. R., Radu, E., & Rúnarsson, H. F. 2015, *PhRvL*, 115, 211102
- Cunha, P. V. P., Herdeiro, C. A. R., Radu, E., Rúnarsson, H. F., & Wittig, A. 2016, *PhRvD*, 94, 104023
- Dolan, S. R., & Shipley, J. O. 2016, *PhRvD*, 94, 044038
- EHT Collaboration, et al. 2019, *ApJL*, 875, L1
- Emel'yanenko, V. V. 2007, *Celest. Mech. Dyn. Astron.*, 98, 191
- Ernst, F. J. 1976, *J. Math. Phys.*, 17, 54
- Feng, K. 1986, *JCM*, 44, 279
- Gao, B., & Deng, X. M. 2021, *Eur. Phys. J. C*, 81, 983
- García, A., Galtsov, D., & Kechkin, O. 1995, *PhRvL*, 74, 1276
- He, G., Huang, G., & Hu, A. 2023, *Symmetry*, 15, 1848
- Hou, Y., Zhang, Z., Yan, H., Guo, M., & Chen, B. 2022, *PhRvD*, 106, 064058
- Hu, A., & Huang, G. 2022, *Universe*, 8, 369
- Hu, A., & Huang, G. 2023, *Symmetry*, 15, 1094
- Huang, L., & Deng, X. M. 2024, *PhRvD*, 109, 124005
- Huang, Z., Huang, G., & Hu, A. 2022, *ApJ*, 925, 158
- Islam, S. U., Kumar, J., Walia, R. K., & Ghosh, S. G. 2023, *ApJ*, 943, 22
- Jayawardana, B., & Ohsawa, T. 2023, *Mathematics of Computation*, 92, 251
- Johannsen, T. 2013, *ApJ*, 777, 170
- Junior, H. C. D. L., Cunha, P. V. P., Herdeiro, C. A. R., & Crispino, L. C. B. 2021, *PhRvD*, 104, 044018
- Karas, V., & Vokrouhlický, D. 1992, *General Relativity and Gravitation*, 24, 729
- Kawashima, T., Ohsuga, K., Takahashi, H. R. 2023, *ApJ*, 949, 101
- Kerr, R. P. 1963, *PhRvL*, 11, 237
- Kopáček, O., & Karas, V. 2018, *ApJ*, 853, 53
- Kopáček, O., Karas, V., Kovár, J., & Stuchlík, Z. 2010, *ApJ*, 722, 1240
- Kološ, M., Tursunov, A., & Stuchlík, Z. 2021, *PhRvD*, 103, 024021
- Kumar, J., Islam, S. U., & Ghosh, S. 2022, *JCAP*, 2022, 032
- Li, D., & Wu, X. 2019, *European Physical Journal Plus*, 134, 96
- Liu, C., & Wu, X. 2023, *Universe*, 9, 365
- Lu, J., & Wu, X. 2024, *Universe*, 10, 277
- Melvin, M. A. 1965, *Phys. Rev. B*, 139, 225
- Mikkola, S. 1997, *Celest. Mech. Dyn. Ast.*, 67, 145
- Mikkola, S., & Tanikawa, K. 1999, *Celest. Mech. Dyn. Ast.*, 74, 287
- Mikkola, S., & Tanikawa, K. 2013, *New Astronomy*, 20, 38

- Ohsawa, T. 2023, *SIAM Journal on Numerical Analysis*, 61 (3), 1293
- Pánis, R., Kološ, M., & Stuchlík, Z. 2019, *Eur. Phys. J. C*, 79, 479
- Pelle, J., Reula, O., Carrasco, F., Bederian, C. 2022, *MNRAS*, 515, 1316
- Pihajoki, P. 2015, *Celestial Mech. Dynam. Astronom.*, 121, 211
- Preto, M., & Saha, P. 2009, *ApJ*, 703, 1743
- Preto, M., & Tremaine, S. 1999, *AJ*, 118, 2532
- Pu, H., Yun, K., Younsi, Z., & Yoon, S. 2016, *ApJ*, 820, 105
- Ruth, R. D. 1983, *ITNS*, 30, 2669
- Seyrich, J., & Lukes-Gerakopoulos, G. 2012, *PhRvD*, 86, 124013
- Stuchlík, Z., M. Kološ, M. 2016, *Eur. Phys. J. C*, 76, 32
- Sun, W., Wang, Y., Liu, F., & Wu, X. 2021a, *Eur. Phys. J. C*, 81, 785
- Sun, X., Wu, X., Wang, Y., Deng, C., Liu, B., & Liang, E. 2021b, *Universe*, 7, 410
- Takahashi, M., & Koyama, H. 2009, *ApJ*, 693, 472
- Tsang, D., Galley, C. R., Stein, L. C., & Turner, A. 2015, *ApJL*, 809, L9
- Tursunov, A., Stuchlík, Z., & Kološ, M. 2016, *PhRvD*, 93, 084012
- Tursunov, A., Stuchlík, Z., Kološ, M., Dadhich, N., & Ahmedov, B. 2020, *ApJ*, 895, 14
- Virbhadra, K. S. 2024, *PhRvD*, 109, 124004
- Virbhadra, K. S., Narasimha, D., & Chitre, S. M. 1998, *Astron. Astrophys.*, 337, 1
- Wald, R. M. 1974, *PhRvD*, 10, 1680
- Wang, M., Chen, S., & Jing, J. 2021d, *PhRvD*, 104, 084021
- Wang Y., Sun W., Liu F., Wu X. 2021a, *ApJ*, 907, 66
- Wang Y., Sun W., Liu F., Wu X., 2021b, *ApJ*, 909, 22
- Wang Y., Sun W., Liu F., Wu, X. 2021c, *ApJS*, 254, 8
- White, C. J. 2022, *ApJS*, 262, 28
- Wisdom, J. 1982, *AJ*, 87, 577
- Wisdom, J., & Holman, M. 1991, *AJ*, 102, 1528
- Wu, X., Wang, Y., Sun, W., & Liu, F. Y. 2021, *ApJ*, 914, 63
- Wu, X., Wang, Y., Sun, W., Liu, F. Y., & Han, W. B. 2022, *ApJ*, 940, 166
- Yang, D., Cao, W., Zhou, N., Zhang, H., Liu, W., & Wu, X. 2022, *Universe*, 8, 320
- Yang, D., Liu, W., & Wu, X. 2023, *Eur. Phys. J. C*, 83, 357
- Yang, D., & Wu, X. 2023, *Eur. Phys. J. C*, 83, 789
- Yoshida, H. 1990, *Phys. Lett. A*, 150, 262
- Younsi, Z., Psaltis, D., Özel, F. 2023, *ApJ*, 942, 47
- Zhang, J., & Xie, Y. 2022, *Eur. Phys. J. C*, 82, 854
- Zhang, H., Zhou, N., Liu, W., & Wu, X. 2021, *Universe*, 7, 488
- Zhang, H., Zhou, N., Liu, W., & Wu, X. 2022, *General Relativity and Gravitation*, 54, 110
- Zhou, N., Zhang, H., Liu, W., Wu, X. 2022, *ApJ*, 927, 160; 2023, *ApJ*, 947, 94

---

This 2-column preprint was prepared with the AAS L<sup>A</sup>T<sub>E</sub>X macros v5.2.

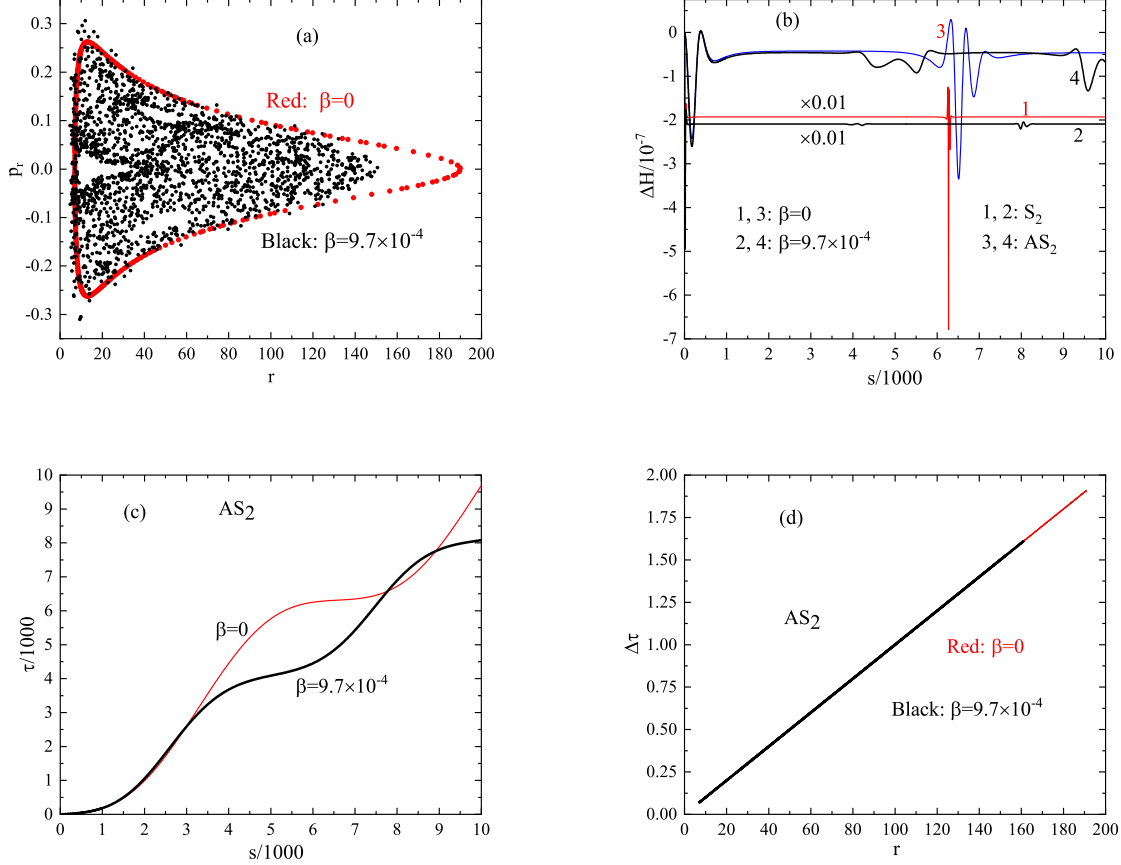


Fig. 1.— Numerical comparisons in between two cases without magnetic field  $\beta = 0$  and with magnetic field  $\beta = 9.7 \times 10^{-4}$  in the Schwarzschild spacetime. (a) Phase space structures of  $r$  and  $p_r$  described by Poincaré section at the plane  $\theta = \pi/2$ . The two algorithms  $S_2$  and  $AS_2$  almost give the same structures. (b) Hamiltonian errors  $\Delta H = H + p_0$ . " $\times 0.01$ " for  $S_2$  means that the plotted errors are the practical ones multiplied by factor 0.01, and " $s/1000$ " represents that the plotted new time  $s$  is the practical one divided by factor 1000.  $s$  is  $\tau$  for  $S_2$ . (c) Relation between the original time  $\tau$  and the new time  $s$ . (d) Different proper time steps  $\Delta\tau$  in different radial separations  $r$  of the orbit for  $\beta = 0$  or  $\beta = 9.7 \times 10^{-4}$ .

Table 1: Effects of different choices of  $j$  on the errors  $\Delta H$  and the proper times  $\tau$ . The orbit with  $\beta = 0$  in Figure 1 is integrated by the method  $AS_2$  until the new time  $s$  reaches 10,000. Only the orders of  $\Delta H$  are listed.  $\tau$  is the proper time at the new time  $s = 10,000$ .

| $j$        | 1                 | 10                | 50                | 100               | 200               | 1000      |
|------------|-------------------|-------------------|-------------------|-------------------|-------------------|-----------|
| $\Delta H$ | $10^{-3}$         | $10^{-5}$         | $10^{-6}$         | $10^{-7}$         | $10^{-8}$         | $10^{-9}$ |
| $\tau$     | $8.6 \times 10^5$ | $9.5 \times 10^4$ | $1.9 \times 10^4$ | $9.7 \times 10^3$ | $5.7 \times 10^3$ | 178       |

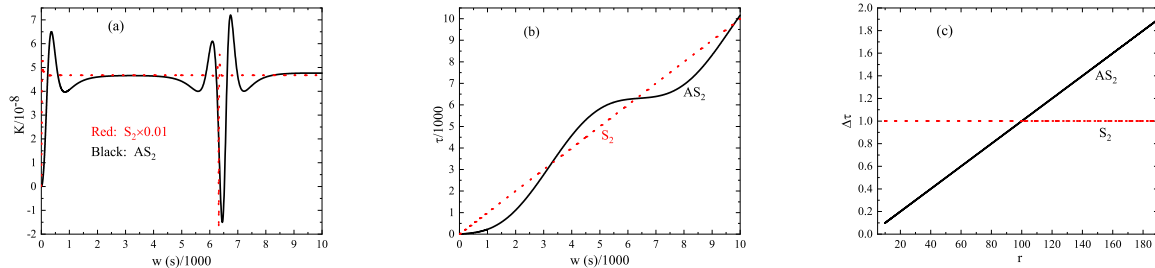


Fig. 2.— Numerical comparisons in between the two methods  $S_2$  and  $AS_2$  integrating the time-like geodesics in the Kerr spacetime. (a) Hamiltonian errors  $K$  of Equation (6). The time is  $w$  for  $S_2$ , and  $s$  for  $AS_2$ . The plotted errors are decreased 100 times for  $S_2$ . (b) Relation between the proper time  $\tau$  and the new time  $w$  or  $s$ . (c) Different proper time steps  $\Delta\tau$  in different radial separations  $r$  of the orbit.

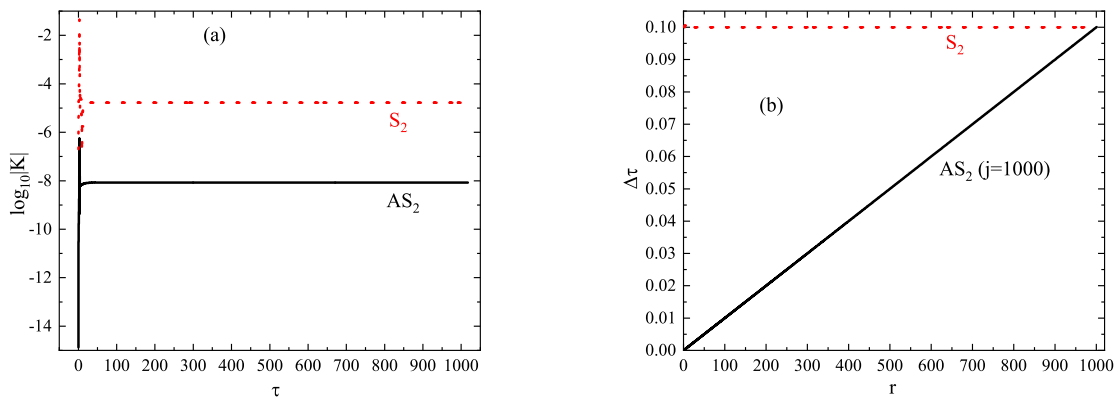


Fig. 3.— Numerical comparisons in between the two methods  $S_2$  and  $AS_2$  integrating the null geodesics in the Kerr spacetime. A photon orbit escaping to infinity has the parameters  $a = 0.3$ ,  $E = 0.99$ ,  $L = 3\sqrt{3}E/10$  and the initial conditions  $r = 3$ ,  $\theta = \pi/2$ ,  $p_r = 0$ . (a) Hamiltonian errors  $K$  depending on the old time  $\tau$ . (b) Different old time steps  $\Delta\tau$  in different radial separations  $r$  of the escaping orbit.

Table 2: Effects of different choices of  $j$  on the errors  $K$  and the new times  $s$ . The escaping photon orbit of Figure 3 is integrated by the method  $AS_2$  until the distance  $r$  reaches 1000. The old time is  $\tau \approx 1,016$ . Only the orders of  $K$  are listed.

| $j$ | 10        | 100       | 500         | 1000      | 2000        |
|-----|-----------|-----------|-------------|-----------|-------------|
| $K$ | $10^{-4}$ | $10^{-6}$ | $10^{-7.5}$ | $10^{-8}$ | $10^{-8.7}$ |
| $s$ | 81        | 811       | 4,052       | 8,103     | 16,205      |

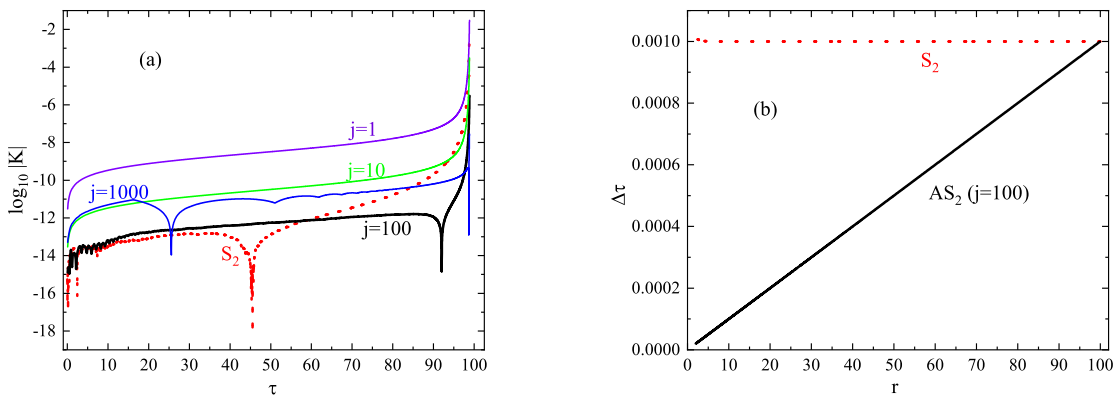


Fig. 4.— Same as Figure 3, but a photon orbit falling into the black hole with the parameters  $a = 0.5$ ,  $E = 0.996$ ,  $L = -2.211$  and the initial conditions  $r = 100$ ,  $\theta = \pi/2$ ,  $p_r = -1.016$  is integrated. (a) Hamiltonian errors  $K$ ; the best choice is  $j = 100$ . (b) Different old time steps  $\Delta\tau$  in different radial separations  $r$  of the falling orbit.

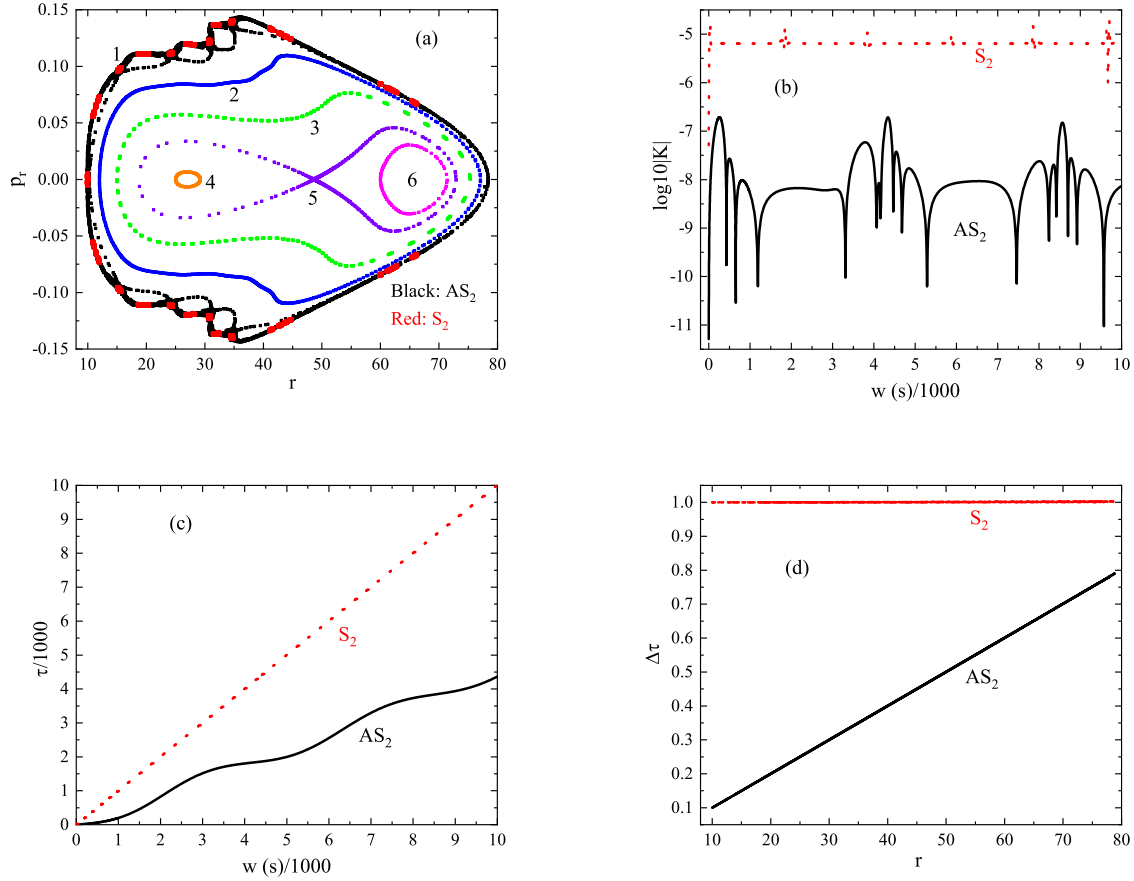


Fig. 5.— Numerical comparisons in simulations of particles around the Schwarzschild-Melvin black hole. The step size is  $h = 1$ , and the parameters are  $E = 0.9905$ ,  $L = 3.6$ ,  $B = 0.001$  and  $j = 100$ . (a) Poincaré section. Orbit 1 with the initial separation  $r = 10$  seems to be regular for  $S_2$  (colored Red), but is weakly chaotic for  $AS_2$  (colored Black). Both methods almost give the same results to any one of Orbits 2-6. (b) Accuracies of Hamiltonian  $K$  in integrations of Orbit 1. (c) Relation between  $w$  (or s) and  $\tau$ . (d) Relation between the proper time step  $\Delta\tau$  and the distance  $r$ .

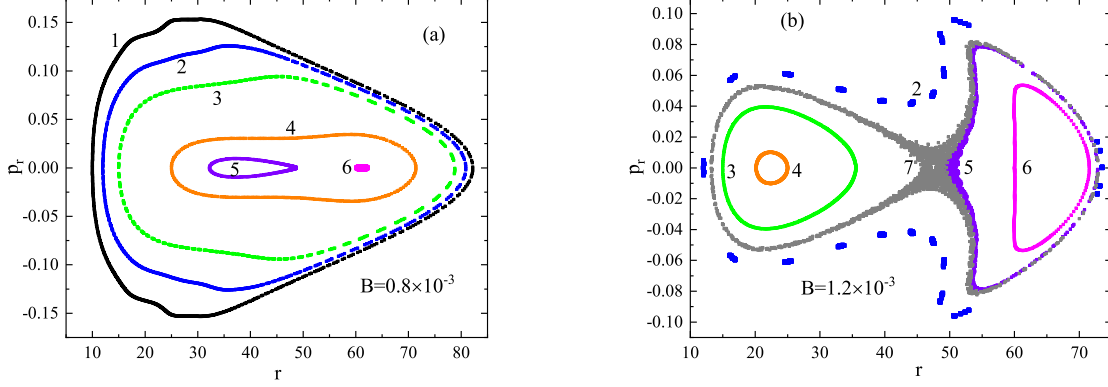


Fig. 6.— Same as Figure 5a but only for the use of  $AS_2$  in two different values of magnetic field parameter  $B$ . (a) In the case of  $B = 0.8 \times 10^{-3}$ , all orbits are regular KAM tori, and the shapes of Orbits 2-6 are unlike those in Figure 5a. (b) When  $B = 1.2 \times 10^{-3}$ , Orbit 5 with the initial distance  $r = 48.7$  and Orbit 7 with the initial distance  $r = 45$  are chaotic.

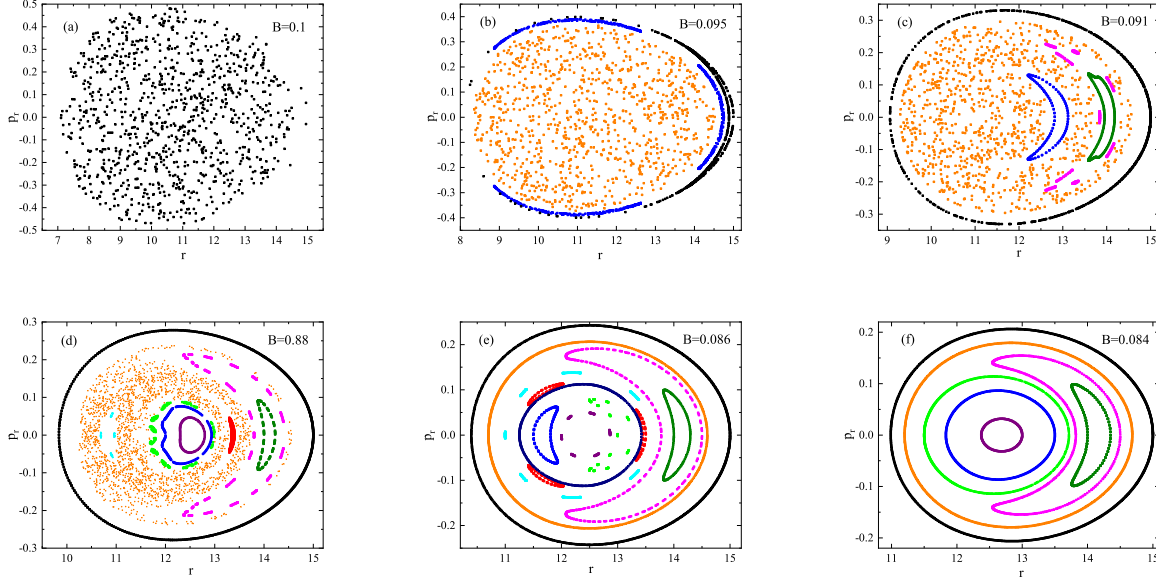


Fig. 7.— Poincaré sections for the motions of photons near the Schwarzschild-Melvin black holes with several values of the magnetic field. The method  $AS_2$  with the step size  $h = 1$  is adopted. The other parameters are  $E = 0.995$  and  $j = 100$ . The angular momentum is always given by  $L = -E \sqrt{-g_{\phi\phi}/g_{tt}}$  with  $r = 15$ . The extent of chaos is weakened as the the magnetic field strength  $B$  decreases in panels (a)-(f).

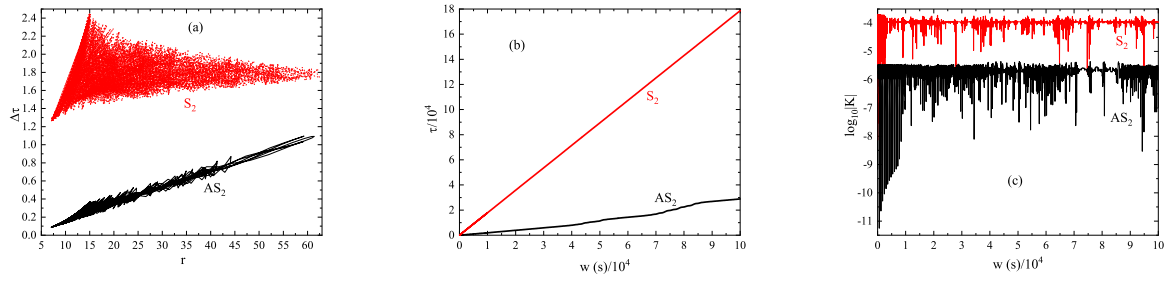


Fig. 8.— Numerical comparisons between the methods  $S_2$  and  $AS_2$  integrating the chaotic photon orbit with the initial separation  $r = 15$  of Figure 7a. The integration step number is  $10^5$ . (a) The old time steps  $\Delta\tau$  depending on the distance  $r$ . (b) The original time  $\tau$  depending on the transformation time  $w$  or  $s$ . (c) Accuracy of Hamiltonian  $K$ .